

# Enhanced structural sensitivity of hybrid-mode acoustic phonons in axially-varying photonic crystal fiber

P. Szriftgiser,<sup>1,\*</sup> A. Kudlinski,<sup>1</sup> D. Bacquet,<sup>1</sup> G. Bouwmans,<sup>1</sup> M. Dossou,<sup>1</sup> J.-C. Beugnot,<sup>2</sup> and V. Laude<sup>2</sup>

<sup>1</sup>Laboratoire PhLAM, UMR CNRS 8523, IRCICA, USR 3380, Université Lille 1, 59655 Villeneuve d'Ascq, France

<sup>2</sup>Institut FEMTO-ST, Université de Franche-Comté and CNRS, 25044 Besançon, France

\*pascal.szriftgiser@univ-lille1.fr

**Abstract:** We report the observation of anti-crossings between hybrid-mode acoustic phonons in an axially-varying photonic crystal fiber. Our experimental results are analyzed using an electrostriction theory which reveals strong coupling between longitudinal and shear components of elastic wave. These anti-crossings are highly sensitive to the transverse fiber structure and thus could be potentially used for ultra-sensitive sensors and new opto-acoustic devices.

©2015 Optical Society of America

OCIS codes: (190.4370) Nonlinear optics, fibers; (290.5830) Scattering, Brillouin.

---

## References and links

1. L. Brillouin, "Diffusion de la lumière et des rayons X par un corps transparent homogène," *Ann. Phys.* **17**, 88–122 (1922).
2. E. P. Ippen and R. H. Stolen, "Stimulated Brillouin scattering in optical fibers," *Appl. Phys. Lett.* **21**(11), 539–541 (1972).
3. R. G. Smith, "Optical power handling capacity of low loss optical fibers as determined by stimulated Raman and Brillouin scattering," *Appl. Opt.* **11**(11), 2489–2494 (1972).
4. X. Bao and L. Chen, "Recent progress in Brillouin scattering based fiber sensors," *Sensors (Basel)* **11**(12), 4152–4187 (2011).
5. P. Russell, "Photonic crystal fibers," *Science* **299**(5605), 358–362 (2003).
6. M. S. Kang, A. Nazarkin, A. Brenn, and P. St. J. Russell, "Tightly trapped acoustic phonons in photonic crystal fibres as highly nonlinear artificial Raman oscillators," *Nat. Phys.* **5**(4), 276–280 (2009).
7. D. Elser, U. L. Andersen, A. Korn, O. Glöckl, S. Lorenz, Ch. Marquardt, and G. Leuchs, "Reduction of guided acoustic wave Brillouin scattering in photonic crystal fibers," *Phys. Rev. Lett.* **97**(13), 133901 (2006).
8. B. Stiller, A. Kudlinski, M. W. Lee, G. Bouwmans, M. Delqué, J.-C. Beugnot, H. Maillotte, and T. Sylvestre, "SBS mitigation in a microstructured optical Fiber by periodically varying the core diameter," *IEEE Photonics Technol. Lett.* **24**(8), 667–669 (2012).
9. M. S. Kang, A. Butsch, and P. St. J. Russell, "Reconfigurable light-driven opto-acoustic isolators in photonic crystal fibre," *Nat. Photonics* **5**(9), 549–553 (2011).
10. P. Dainese, P. St. J. Russell, N. Joly, J. C. Knight, G. S. Wiederhecker, H. L. Fragnito, V. Laude, and A. Khelif, "Stimulated Brillouin scattering from multi-GHz-guided acoustic phonons in nanostructured photonic crystal fibres," *Nat. Phys.* **2**(6), 388–392 (2006).
11. C. G. Poulton, R. Pant, and B. J. Eggleton, "Acoustic confinement and stimulated Brillouin scattering in integrated optical waveguides," *J. Opt. Soc. Am. B* **30**(10), 2657–2664 (2013).
12. K. Furusawa, Z. Yusuoff, F. Poletti, T. M. Monro, N. G. R. Broderick, and D. J. Richardson, "Brillouin characterization of holey optical fibers," *Opt. Lett.* **31**(17), 2541–2543 (2006).
13. B. Stiller, S. M. Foaleng, J.-C. Beugnot, M. W. Lee, M. Delqué, G. Bouwmans, A. Kudlinski, L. Thévenaz, H. Maillotte, and T. Sylvestre, "Photonic crystal fiber mapping using Brillouin echoes distributed sensing," *Opt. Express* **18**(19), 20136–20142 (2010).
14. J.-C. Beugnot and V. Laude, "Electrostriction and guidance of acoustic phonons in optical fibers," *Phys. Rev. B* **86**(22), 224304 (2012).
15. V. Laude and J.-C. Beugnot, "Generation of phonons from electrostriction in small-core optical waveguides," *AIP Adv.* **3**(4), 042109 (2013).
16. S. Diaz, S. Foaleng Mafang, M. Lopez-Amo, and L. Thevenaz, "A high-performance optical time-domain Brillouin distributed fiber sensor," *IEEE Sens. J.* **8**(7), 1268–1272 (2008).

17. M. Dossou, D. Bacquet, and P. Sznitgiser, "Vector Brillouin optical time-domain analyzer for high-order acoustic modes," *Opt. Lett.* **35**(22), 3850–3852 (2010).
18. F. Mihélic, D. Bacquet, J. Zemmouri, and P. Sznitgiser, "Ultrahigh resolution spectral analysis based on a Brillouin fiber laser," *Opt. Lett.* **35**(3), 432–434 (2010).
19. K. Shiraki, M. Ohashi, and M. Tateda, "Suppression of stimulated Brillouin scattering in a fibre by changing the core radius," *Electron. Lett.* **31**(8), 668–669 (1995).
20. J. Yu, I.-B. Kwon, and K. Oh, "Analysis of Brillouin frequency shift and longitudinal acoustic wave in a silica optical fiber with a triple-layered structure," *J. Lightwave Technol.* **21**(8), 1779–1786 (2003).
21. L. Zou, X. Bao, S. Afshar V, and L. Chen, "Dependence of the Brillouin frequency shift on strain and temperature in a photonic crystal fiber," *Opt. Lett.* **29**(13), 1485–1487 (2004).
22. C. M. Smith, N. Venkataraman, M. T. Gallagher, D. Müller, J. A. West, N. F. Borrelli, D. C. Allan, and K. W. Koch, "Low-loss hollow-core silica/air photonic bandgap fibre," *Nature* **424**(6949), 657–659 (2003).

## 1. Introduction

Stimulated Brillouin scattering (SBS) is an inelastic process in which acoustic phonons of a medium interact with photons propagating through it [1]. In optical fibers, light excites acoustic waves via electrostriction, which results in the amplification of a frequency down-shifted backward radiation [2]. This process is well known to high-power laser scientists, since it sets a severe limitation upon the maximal power that can be transmitted through an optical fiber [3]. In contrast, it can be efficiently used to design smart all-fiber distributed sensors for strain, temperature, or other physical quantities [4]. Recently, artificially structured photonic crystal fibers (PCFs) [5] have brought in unprecedented opto-acoustic properties, spurring a renewal in both fundamental and applied research in sound-light interactions. Breakthroughs brought by PCF technology include the observation of Raman-like transitions [6], the reduction of forward guided acoustic wave Brillouin scattering (GAWBS) noise in quantum-optics experiments [7], the reduction of photon/phonon coupling efficiency by periodically varying the air-hole microstructure [8], the demonstration of reconfigurable all-optical isolation [9], and the observation of hybrid-mode phonons resulting from the combination of shear and longitudinal strain [10], with great potential for tight confinement of acoustic waves [11].

In optical fibers, SBS is commonly considered as resulting of the interaction of photons with longitudinal phonons, similar to the scattering of plane waves in bulk silica. This process gives structural information regarding the optical fiber inside which it is occurring. The Brillouin Stokes frequency shift  $\nu_B$  ( $\sim 10$  GHz for 1550 nm light in silica fibers) is given by

$$\nu_B = 2 \frac{n_{eff} V_a}{\lambda_p} \quad (1)$$

where  $n_{eff}$  is the effective optical index,  $V_a$  is the phonon velocity, and  $\lambda_p$  is the pump wavelength. SBS is an ideal backward process with gain that is thus accessible to pump-probe and reflectometry experiments. Structural information can be retrieved from Eq. (1) as  $\nu_B$  is proportional to  $n_{eff}$ , that is itself linked to the fiber transverse geometry [12,13]. A difficulty with SBS is that  $\nu_B$  - through either  $n_{eff}$  or  $V_a$  - is also sensitive to many other physical quantities such as temperature, longitudinal strain, birefringence, or doping concentration. Discriminating structural variations from other fluctuations requires more information. As shown by Dainese and *al.*, PCF with a small core supports hybrid acoustic modes (HMs) having a polarization that is a mixture of longitudinal and shear displacements [10]. Thanks to the longitudinal component, HMs are SBS active. As their exact modal distribution depends acutely on the holey distribution surrounding the core, HMs potentially present enhanced structural sensitivity.

In the present work, thanks to a slow and precise grading of the scale of the transverse structure of the fiber, we gain a new degree of control on light-sound interactions in the already versatile PCF platform. This tapered fiber unveils highly unusual anti-crossings between different hybrid-mode acoustic phonons. Two different SBS active phonons are

furthermore identified. An electrostriction model [14,15] explains their generation from optical forces generated by light travelling along the fiber. Both phonons are found to be of the HM type. One is strongly confined to the core, while the other extends up to the holey structure and is dramatically sensitive to structural variations.

## 2. Properties of the tapered PCF

We consider in this work a PCF with continuously adjusted transverse dimension, whose variation is carefully controlled during drawing. The outer diameter profile of the fiber was measured during drawing and is displayed in Fig. 1(b). The PCF is made of a  $\sim 170$  m-long segment with an outer diameter increasing linearly from  $80\ \mu\text{m}$  to  $135\ \mu\text{m}$ , followed by a uniform  $\sim 48$  m-long segment with a  $135\ \mu\text{m}$  outer diameter. For such a slowly tapered fiber, the fabrication tolerance is similar to uniform fibers: the outer diameter is controlled with a typical accuracy of  $\pm 0.5\ \mu\text{m}$ . Scanning electron microscope (SEM) images of each section are reported in Figs. 1(a) and 1(c) with the same scale, for the input (small diameter) and the output (large diameter) cross-sections. For the smallest section, the hole-to-hole spacing (pitch  $\Lambda$ ) and core diameter  $D$  are  $1.55\ \mu\text{m}$  and  $2.14\ \mu\text{m}$ , respectively. For the largest section, they are  $2.52\ \mu\text{m}$  and  $3.57\ \mu\text{m}$ , respectively.

The PCF core is highly doped with germanium (Ge), with a parabolic distribution and a maximum refractive index difference  $\Delta n = 0.032$ . The reason to use a Ge-doped core is that it enhances the confinement of the optical field in the core. The doped areas can be seen as the light grey regions at the center of the core in Figs. 1(a) and 1(c). The refractive index profile of the doped core is shown in Fig. 1(d) for both the smallest section (black line) and the largest one (red line). The left axis presents the corresponding evolution of the glass density across the core, as used in the numerical simulations presented in the manuscript. Figure 1(e) shows the longitudinal (“L”) and shear (“S”) acoustic velocities across the Ge-doped core, again for both the smallest section (black line) and the largest one (red line). The calculated effective index  $n_{eff}$  of the fundamental optical mode equals 1.4007 and 1.4273 at  $1.55\ \mu\text{m}$  for the smallest and the largest section, respectively. We checked numerically that the fiber is optically single mode throughout its length. For intermediate distances,  $n_{eff}$  is assumed to follow linearly the scale of the holey structure.

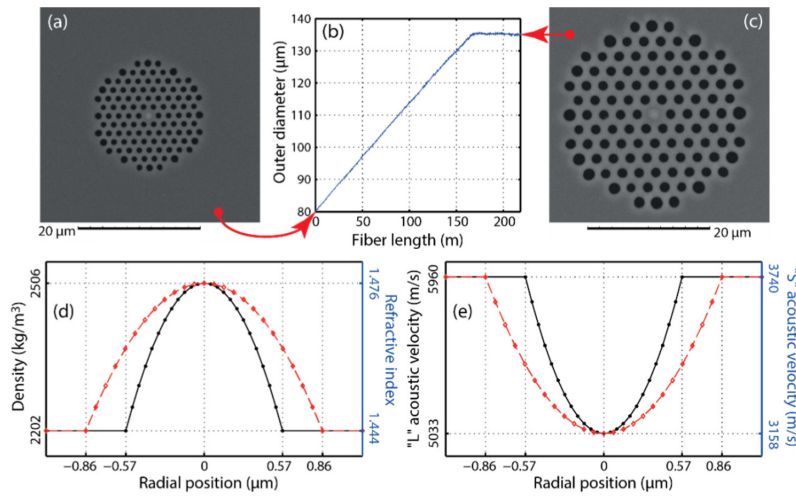


Fig. 1. (a) and (c) SEM pictures of the PCF observed at its smallest (a) and its largest (c) section (shown with the same scale). (b) Evolution of the PCF outer diameter versus length as measured during drawing. (d) Density (left axis) and refractive index (right axis) across the germanium doped core. (e) “L” longitudinal (left axis) and “S” shear (right axis) acoustic velocities across the germanium doped core. In (d) and (e), black solid lines correspond to the small section and red dashed lines to the large one.

After our experiments, the PCF was cut back in 10 m long samples and the transverse structure of each segment was analyzed with a SEM, confirming that the PCF structure was homothetically conserved (within experimental accuracy) all along the fiber.

### 3. Experimental setup

The PCF was characterized with a Brillouin optical time-domain analyzer (BOTDA) [16]. The principle of the measurement is to launch a pulsed pump in the fiber, and to log the time of flight of a backward continuous probe with a given red shift detuning. Here, we use a vector version of BOTDA (VBOTDA) [17]. The advantage of the vector configuration is twofold. First, detection is performed at high frequency. It is thus highly immune to low frequency noise, allowing for detection of HMs that are several orders of magnitude less intense than the main Stokes line. Second, spectrograms can be demodulated to yield the phase of the Brillouin interaction.

In our experimental setup, the emission of a low noise distributed-feedback laser diode, whose typical spectrum can be found in [18], is split into two separate paths. One path is pulsed and amplified to generate the pump (1.1 W, 50 ns long pulses, resulting in a  $\Delta z_{pulse} \sim 5$  m spatial resolution). The other path is modulated to generate sidebands for the probe. In the VBOTDA configuration, a phase rather than an intensity modulator is used. The phase modulator is furthermore driven by two distinct frequencies. The first frequency is arbitrarily set at  $f_{LO} = 2$  GHz, while the other one,  $f_s$ , is tuned so that the probe sideband at  $f_{probe} = -(f_s + f_{LO})$  can be scanned throughout the chosen resonance. After travelling through the fiber, the probe detection is made at 2 GHz. If — assuming a perfect phase modulation scheme — the  $f_{probe}$  sideband is far from any resonance, it is not amplified, and no intensity modulation is detected. When  $f_{probe}$  enters a resonance, it is amplified and the phase modulation equilibrium is broken. A 2 GHz beat-note between the  $f_{probe}$  and  $-f_s$  sidebands appears, leading to a 2 GHz intensity modulation. This signal is sampled at a 10 GHz rate with a high speed oscilloscope. It is then sliced into segments made of  $N_{FFT} = 64$  (unless otherwise stated) consecutive points, *i.e.* a  $\Delta z_{num} = \sim 32$  cm numerical resolution. This value takes into account the fact that to optimize  $\Delta z_{num}$ , each segment has a 50% overlap with the previous one. The amplitude and the relative phase of each segment at 2 GHz are then extracted with a fast Fourier transform.

### 4. Results

In the present experiments, both PCF ends were spliced to conventional 1.55  $\mu\text{m}$  single-mode fiber pigtails and the laser pump was launched at the fiber extremity with smallest diameter. Experimental spectrograms (averaged 256 times) are reported in Fig. 2 with a double horizontal axis showing both the distance along the fiber (bottom) and the local pitch  $\Lambda$  (top). Figures 2(c) and 2(d) present the experimental intensity and phase spectrograms, respectively. In addition to the expected main resonance (labelled HM0 in this work) observed around  $\sim 9.9$  GHz, a weaker set of resonances (labelled HM1) is observed at higher frequencies, around 10.9 GHz. Figures 2(a) and 2(b) are close-up views on HM1 resonances around the 10.9 GHz region of the acoustic spectrum. As discussed below, these resonances appear at the frequency of distinct HMs. The HM1 line is less intense than the HM0 line by an intensity factor of 11 to 26 dB, depending on distance. For both lines, a frequency correlation with distance (and thus with the PCF structure) clearly appears.

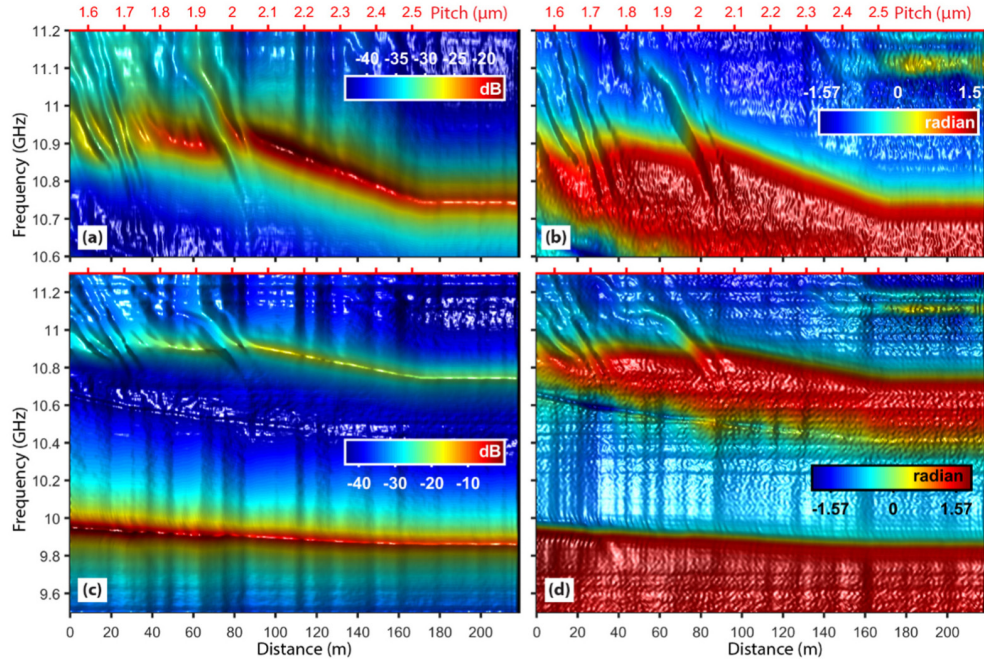


Fig. 2. (a) and (c) Experimental relative intensity spectrogram (in dB) as a function of fiber distance. (b) and (d) Corresponding phase spectrograms (in radians). (a) and (b) are close-ups on the higher frequency (HM1) component experiencing anti-crossings. Top abscissa axis: pitch  $\Lambda$  (in  $\mu\text{m}$ ) for the tapered section.

Let us first focus on the main resonance (HM0). As expected, the HM0 frequency is modified as the fiber diameter changes. Intuitively, as  $n_{\text{eff}}$  increases with diameter along the first 170 meters, it would be expected from Eq. (1) that the Brillouin frequency increases correspondingly. The opposite, however, is observed in Fig. 2(c): the HM0 frequency decreases while the diameter, and hence  $n_{\text{eff}}$ , increases. This was observed previously in standard fibers and was attributed to doping [19,20]. Indeed, the explanation can be found by looking at Visualization 1, which shows the evolution of the fundamental optical mode (left), the HM0 mode (middle) and the HM1 mode (right) as a function of decreasing pitch (and thus diameter). As the diameter becomes smaller, both the fundamental optical mode (left panel) and the HM0 acoustic mode (middle panel) spread more widely in the fiber structure. The overlap with the Ge-doped area thus decreases, so that the usual assumption that  $V_a$  is constant is not valid anymore. As the acoustic velocity  $V_a$  in pure silica is higher than in the Ge-doped core, as shown in Fig. 1(e),  $v_B$  might increase even if  $n_{\text{eff}}$  decreases, and the phonon velocity shift can override the optical index decrease. In the limit that the fiber is not doped with Ge, one should recover Eq. (1) with constant  $V_a$ .

Let us now consider the second resonance HM1 located around 10.9 GHz. Its evolution with fiber length strongly differs from that of the main resonance HM0. Indeed, for small pitch values ( $\Lambda < \sim 2.1 \mu\text{m}$ ) within the first 100 m of the fiber, the evolution of the resonance frequency appears to be quite complex both in intensity, and phase, Figs. 2(a) and 2(b). The intensity of the SBS signal almost vanishes for several frequencies, which is accompanied by strong changes in the slope of resonance frequency versus distance. Similar observations were made in a range of PCF samples with slightly different holey structures, hence ruling out fabrication errors and possible artefacts.

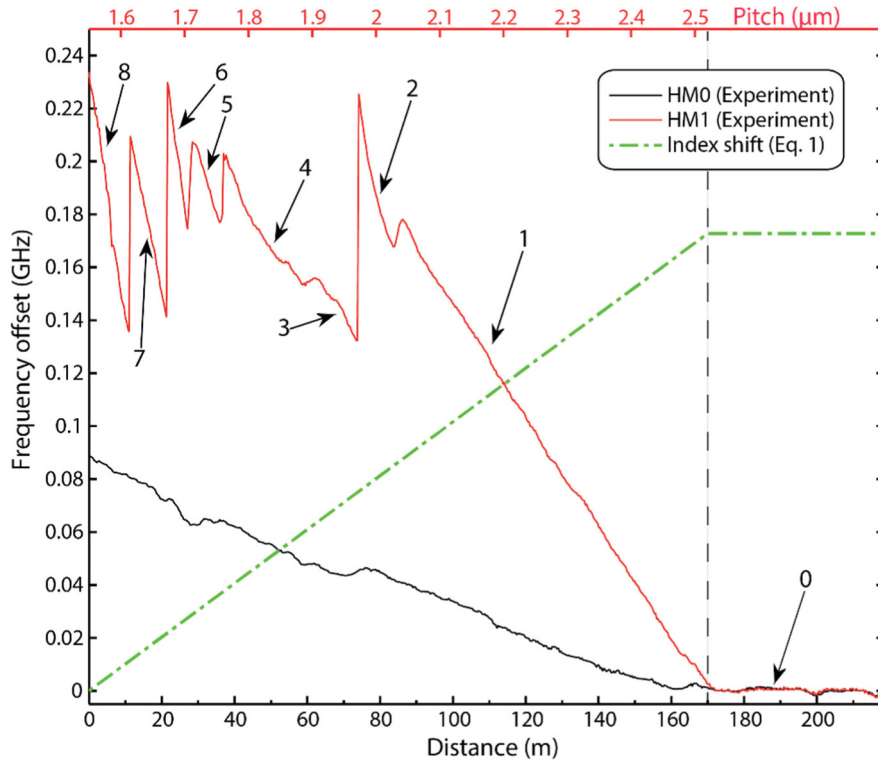


Fig. 3. Measured relative frequency shift of HM0 and HM1 phonons (black and red lines respectively) as a function of distance along the PCF. Top axis: local pitch  $\Lambda$  in  $\mu\text{m}$ .

Figure 3 shows the evolution of HM0 (black line) and HM1 (red line) frequencies with fiber length (bottom axis) and microstructure pitch  $\Lambda$  (top axis) extracted from the intensity spectrograms of Fig. 2(c) (data extracted from the experimental phase spectrogram give comparable results, but are slightly noisier and are not shown here). The evolution of the HM1 frequency with fiber length is highly unusual as it exhibits discontinuities and strong changes of their slope, which highlights their enhanced sensitivity to structural parameters as compared to the HM0 resonance, a striking feature! Indeed, although it is expected that a slow variation of the fiber structure slightly changes the Brillouin frequency, as observed for HM0, the strong variation of HM1 frequency comes as a surprise. The fiber length is labelled into different regions according to these features. In addition to the uniform region labelled “0”, at least eight different regions, each corresponding to a different HMs, are identified. Their geometrical resolutions  $R_{1..8}$  with respect to  $\Lambda$  and  $n_{\text{eff}}$  (in refractive index unit, RIU) are summarized in Table 1 for the HM1 resonance. In particular, the sensitivity of HM1 in the region labelled “6” is as high as  $R_6 = -64.3 \text{ GHz/RIU}$  ( $-1.76 \text{ GHz}/\mu\text{m}$ ), which is in absolute value 20 times higher than the one of the HM0 resonance (of  $-3.3 \text{ GHz/RIU}$ , or equivalently  $-0.09 \text{ GHz}/\mu\text{m}$ ). The most sensitive resolution ( $-1.76 \text{ GHz}/\mu\text{m}$ ) with respect to  $\Lambda$  corresponds to a  $\sim 0.6 \text{ nm}$  resolution if one considers that the VBOTDA minimum frequency resolution is  $1 \text{ MHz}$ . The actual resolution is probably even better, because the distance along which this mode was excited ( $\sim 5.5 \text{ m}$ ) was equal to the apparatus spatial resolution limit  $\Delta z_{\text{pulse}} \sim 5 \text{ m}$  (which was not optimized here).

**Table 1. Geometrical frequency resolution of HM0 and the various HM1 acoustic phonons appearing along the fiber, as labelled in Fig. 3. Second line: resolution versus the effective index,  $n_{eff}$ . Third line: resolution versus the fiber pitch,  $\Lambda$ .**

	HM0	$R_1$	$R_2$	$R_3$	$R_4$	$R_5$	$R_6$	$R_7$	$R_8$
GHz/RIU	-3.3	-13.4	-38.0	-11.8	-13.0	-30.0	-64.3	-43.4	-61.0
GHz/ $\mu\text{m}$	0.09	-0.37	-1.04	-0.32	-0.36	-0.82	-1.76	-1.19	-1.67

## 5. Discussion

In order to understand the unusual behavior of the HM1 resonance evolution with fiber structure, we modelled electrostriction in the PCF following the theory of Ref [15]. Figure 4 reports the calculated intensity spectrogram as a function of the fiber pitch. SBS-generated acoustic phonons are obtained by solving the elasto-dynamic equation subject to the optical forces that arise from the distribution of light within the fiber cross-section, as a result of electrostriction at the detuning frequency. With this approach, because the fundamental optical mode is confined to the core of the fiber, optical forces and hence generated acoustic phonons are obtained right where the interaction takes place [14], without need to resort to a full band structure computation [10,21]. The starting and ending points of the numerical simulation of Fig. 4 are the two fiber sections displayed in Fig. 1(a) and 1(c), with a linear scaling of the fiber structure in between. The purpose of the computation is not to reproduce exactly experimental data – which would be quite difficult, given the uncertainties in actual PCF parameters, – but rather to recover a general picture of the underlying physics. Indeed, one can see from Fig. 4 that the general shape of the numerical spectrogram is in good qualitative agreement with the experimental one. Resonances HM0 and HM1 are well identified around 9.9 GHz and 10.9 GHz, respectively, and the evolution of their frequencies with distance (i.e., the fiber structure) as well as their slopes are in reasonable agreement with experimental values. The polarization of HM0 (respectively, HM1) is calculated to be around 90% (resp., 75%) longitudinal and 10% (resp., 25%) shear, with 4% (resp. 10%) variation of this content along the fiber. The HM0 line displays no particular events, except for the unusual variation of Brillouin frequency with fiber structure discussed above. The computation also qualitatively confirms the complex and intriguing dynamics of the HM1 resonance for small pitch values.

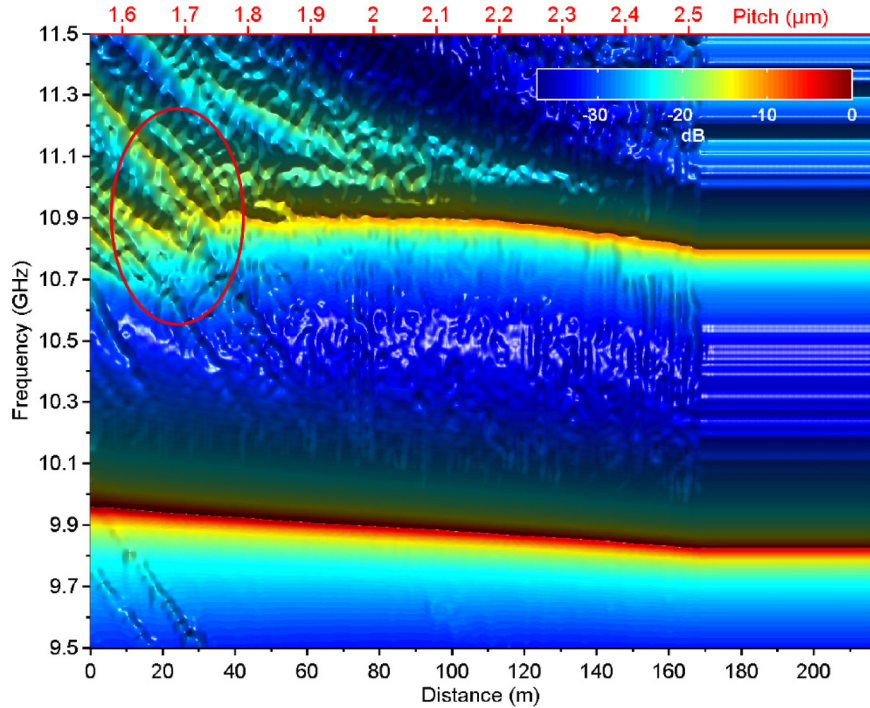


Fig. 4. Numerical spectrogram versus equivalent distance (bottom axis) or pitch  $\Lambda$  in  $\mu\text{m}$  (top axis). In order to simulate a uniform section, identical data are replicated beyond a distance of 170 m. A closer view of the anti-crossing inside the red ellipse is reported Fig. 5(g) with higher numerical resolution.

To get further insight into this dynamics, Fig. 5(g) shows a high resolution close-up view of the numerical spectrogram displayed in Fig. 4, for pitch values around  $1.7 \mu\text{m}$ . This figure suggests, in accordance with the experimental results of Fig. 2, that the HM1 line represented in red line in Fig. 3 does not correspond to a single phonon, but rather results from a series of hops between different phonon branches. The frequency dependence with fiber structure of these phonons exhibits either a moderate or a steep slope. Because of different dependences with fiber structure, there is a particular structure size for which two successive phonons have the same phase velocity, causing anti-crossings to occur. This phenomenon occurs several times, *i.e.* for several structure sizes, in experimental as well as in numerical data, suggesting that different HM1 phonons are involved in the process each time an anti-crossing occurs. Besides, the spectrogram of Fig. 5(g) indicates that the phenomenon is actually quite complex. Because HM1 phonons are continuously appearing and disappearing, the dispersion at the anti-crossing point does not exhibit, in this case, the classical “X” shape, as in usual anti-crossings between purely optical core and optical surface modes in hollow core photonic bandgap fibers, for instance [22]. Instead, it has an asymmetric “Y” shape in our case, with some energy located in between the two main branches, see Fig. 5(g), which emphasizes the complexity of the HM1 phonons dynamics.

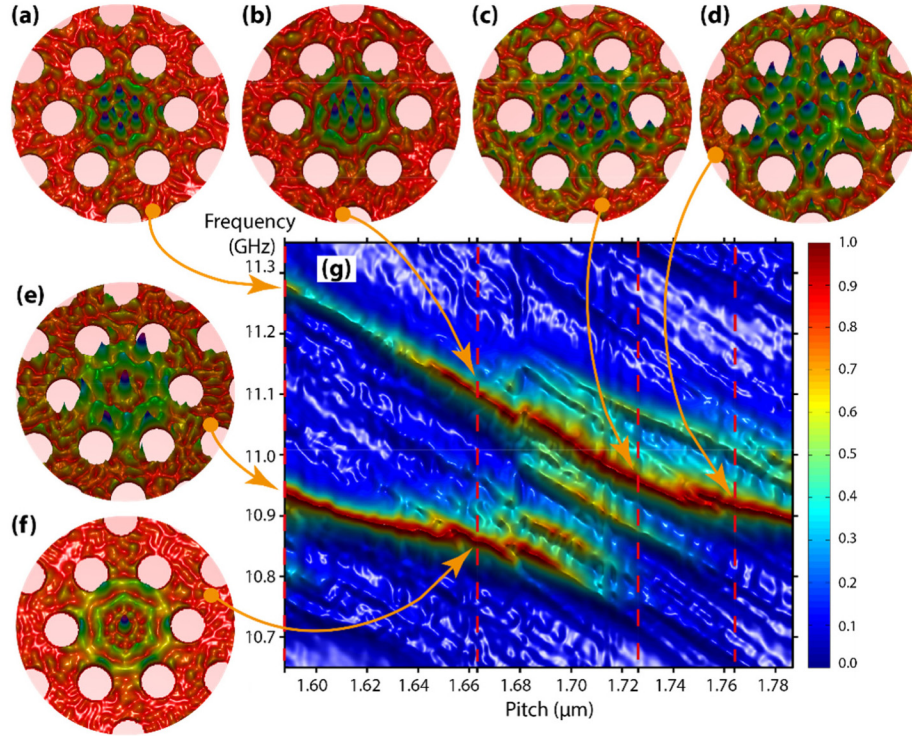


Fig. 5. (g) Close-up view at the anti-crossing appearing in Fig. 4 around a distance of 20 m. (a-f) Normalized acoustic kinetic energy distribution for different HM phonons selected along the two main branches of the anti-crossing. [Visualization 1] left to right: cross section of the fundamental optical mode (left), kinetic acoustic energy distribution of the HM0 mode (middle), and kinetic acoustic energy of the HM1 most intense mode, as a function of decreasing pitch (and thus fiber diameter).

In order to numerically validate the existence of an anti-crossing from simulations of Fig. 4, we computed the radial complex acoustic amplitude distribution  $|n\rangle$  ( $n = a, b, \dots, f$ ) for several modes taken along the two main branches of the “Y” in Fig. 5(g). Their norms are displayed in Figs. 5(a)-5(f), and the associated Visualization 1 shows their full evolution with fiber pitch. The overlap integral  $\langle m|n\rangle$  of two modes  $|n\rangle$  and  $|m\rangle$  may be estimated as by

$$\langle m|n\rangle = \iint m^*(x, y)n(x, y)dx dy \quad (2)$$

where the symbol “\*” indicates the complex conjugate operation, and  $x$  and  $y$  are dimensionless spatial coordinates in the transverse plane (normalized to the local pitch). Moreover, in Eq. (2), each mode amplitude is normalized so that  $\langle m|m\rangle = \langle n|n\rangle = 1$ . We found that  $|\langle e|a\rangle| \sim 0.08$ , which is quite low. This is not surprising, however, since  $|a\rangle$  and  $|e\rangle$  lie on different branches far from the anti-crossing center located around  $\Lambda = 1.7 \mu\text{m}$ ; they are therefore expected to be independent, with a low overlap. Conversely, we checked that the absolute value overlap of two adjacent modes lying on the same branch is much larger. For instance, we found on the upper frequency branch  $|\langle a|b\rangle| \sim 0.38$ ,  $|\langle b|c\rangle| \sim 0.57$ , and  $|\langle c|d\rangle| \sim 0.49$ , while we found on the lower frequency branch  $|\langle e|f\rangle| \sim 0.50$ . Now, considering the overlap of  $|e\rangle$  and  $|d\rangle$ , two modes that lie on either side of the anti-crossing, we found a significant value of  $|\langle e|d\rangle| \sim 0.28$ . This means that after the high frequency branch inflexion point, modes that were initially independent ( $|\langle e|a\rangle| \sim 0.08$ ) are now partially mixed, which constitutes a clear sign of an anti-crossing. This analysis is further emphasized in the media file associated to Fig. 5, which shows that the spatial distribution of the HM1 mode indeed

varies very strongly with the fiber structure for pitch values between 1.6 and 1.8  $\mu\text{m}$  (at the end of the movie).

More generally, anti-crossings are a universal nature feature that is not restricted to a complex fiber structure. For instance, Fig. 3 in reference [10] reports a numerical simulation for a solid rod that also displays acoustic anti-crossings. (Since there is no hole, the modes behavior is much simpler). Therefore, Ge doping is not mandatory for the existence of the HM1 anti-crossing. However the experimental observation of anti-crossing in PCF doped fiber is much easier because the Ge core reduce the number of resonances at high frequencies.

From the point of view of potential applications, since they are very sensitive, we do not know how HM1 anti-crossings might be shifted from one particular fiber to another one. This is beyond the scope of the present work. We have however observed that the spectrogram displayed in Fig. 2 is very stable over time for a given fiber. If it might be difficult to accurately predict their appearance for a given pitch of the fiber, it thus seems clear that the very existence of anti-crossings is very robust.

To conclude this discussion, one might think of new potential applications: if a fiber displays more than one hybrid phonon mode, there are also more information at hand. One could then think to fabricate a holey fiber with a uniform diameter. On the one hand, if the most intense HM1 mode is not too close from an anti-crossing, this fiber could be used for multi-dimensional distributed strain sensing. Actually, a transverse pressure will in turn induce a transverse fiber geometrical deformation that could be sensed by an HM1 mode. Simultaneously and almost independently, HM0 could sense the usual longitudinal strain. Since the sensitivity of HM0 to the transverse geometry is low, it should be easy to uncouple the results. On the other hand, if the most intense HM1 mode is very close to an anti-crossing, a tiny localized pressure could commute the most intense HM1 mode. This would thereby provide a line of distributed switches.

## 6. Conclusion

To summarize, we have demonstrated that axially-varying photonic crystal fibers provide a new degree of freedom in manipulating and using sound-light interactions through stimulated Brillouin scattering. We have highlighted the presence of anti-crossings between different hybrid-mode acoustic phonons occurring for specific structure dimensions which display a dramatically enhanced geometrical sensitivity in a slowly axially-varying photonic crystal fiber. Besides the universal physics behind the complex features of these anti-crossings, their exalted sensitivity to geometry could be potentially used for ultra-sensitive sensors and new opto-acoustic devices.

## Acknowledgments

The Authors acknowledge Dominique Delande for helpful discussions. This work was partly supported by the “Fonds Européen de Développement Economique Régional”, the Labex CEMPI (ANR-11-LABX-0007) and Equipex FLUX (ANR-11-EQPX-0017) through the “Programme Investissements d’Avenir”. JCB and VL acknowledge funding from the European Community’s Seventh Framework Programme (FP7/2007-2013) under grant agreement number 233883 (TAILPHOX).